Letter   Editors' Suggestion

Buckling kinetics of graphene membranes under uniaxial compression

Aristotelis P. Sgouros [*], Evangelos Drougkas,[†] Spyros V. Kallivokas [‡] and Doros N. Theodorou

School of Chemical Engineering, National Technical University of Athens,
9 Heroon Polytechniou Street, Zografou Campus, GR-15780 Athens, Greece

Despite past investigations of the buckling instability, the kinetics of the buckling process is not well understood. We develop a generic framework for determining the buckling kinetics of membranes under compressive stress (σ_b) via molecular dynamics simulations. The buckling time (t_b) is modeled by an extended Boltzmann-Arrhenius-Zhurkov equation accounting for temperature (T) and scale-dependent bending rigidity. We discern three regimes: (I) t_b decreases with T; (II) t_b increases with T; (III) t_b is T independent. Regime II coheres with the predictions of the theory of fluctuating sheets (TFS). Regime I is seen at small scales due to fluctuations about equilibrium and is not predicted by the TFS.

Understanding the stability of membranes and the mechanisms responsible for wrinkle formation [1–4] is crucial for the design of nanodevices and nanocomposite materials for electronic [5–7], thermal management [8], strain engineering [1–3,9,10], and biological [5,11–13] applications.

The elastic properties of slender plates are well-understood [14–16]; however, as we move towards the atomistic regime they become scale-dependent due to the onset of thermally induced height fluctuations [17–25]. According to the theory of fluctuating sheets (TFS) [17–20,26], the height fluctuations $\langle h^2 \rangle$ depend on the ratio of the lateral dimensions of the sheet (l_T) in relation to the thermal length:

$$l_{th} = 2\pi\sqrt{16\pi\kappa_0^2/(3k_B T E_0^{2D})} \sim T^{-0.5} \tag{1}$$

with E_0^{2D} being the two-dimensional (2D) Young's modulus and κ_0 the bending rigidity at 0 K; note that, $\lim_{T\to 0} l_{th} = \infty$. If $l_T \ll l_{th}$ the elastic constants remain unaffected, whereas if $l_T \gg l_{th}$, the (renormalized) elastic constants become scale-dependent. Hereafter, a (renormalized) physical property $\mathcal{A}$ at zero (finite) temperature will be denoted with $\mathcal{A}_0$ ($\mathcal{A}$).

E^{2D} decreases with increasing size: $E^{2D}/E_0^{2D} \sim (l_T/l_{th})^{-2+2\eta}, l_T \gg l_{th}$; where $\eta \sim 0.8 - 0.85$ [17,18,24,25]. At finite temperatures, part of the applied energy during a tensile (compressive) experiment is spent towards suppressing (promoting) the thermally induced ripples. Conversely, at $T = 0$, the membranes remain planar and the applied stress

deforms the intramolecular bonds and bond-bending angles; hence, yielding higher E^{2D}. κ describes the resistance of the material to bending deformation and increases with slab thickness [14–16]. The thermally induced ripples increase the effective thickness of the sheet; thus, κ increases with size: $\kappa/\kappa_0 \sim (l_T/l_{th})^\eta, l_T \gg l_{th}$.

Assuming that the stretching and bending modes are uncoupled (harmonic approximation), the height fluctuations scale with length as $\langle h^2 \rangle \sim l_T^2$ [19] and the membranes are expected to crumple. However, graphene and other 2D materials are in fact stable at finite T [19,27,28]. Based on the assumption that the stretching and bending modes are coupled (anharmonic approximation), the TFS predicts that, $\langle h^2 \rangle \sim l_T^{2-\eta}$ [18,29]; $\langle h^2 \rangle$ is small relative to the sheet dimensions and the latter can be treated as approximately flat. According to Monte Carlo simulations [29], the scaling predictions of the aforementioned theories are valid only for small graphene sheets with dimensions below ~ 4 nm. With increasing l_T, the scaling predictions break down and graphene features a tendency for ripple formation at a preferred length scale of $\sim 8 - 9$ nm [29,30], in accordance with experiments [31].

Graphene cannot sustain high compressive stresses and its buckling resistance depends on interplay between stretching and bending. The limiting stress along the loading direction x for the onset of the buckling instability is related to κ as

$$\sigma_{lim}^{TFS} \sim \kappa(l_x)l_x^{-2}. \tag{2}$$

Henceforth, we will invoke the convention used on compression experiments [20,32–36] where the compressive stress and strain are reported with positive signs.

If the sheet is small, the thermal fluctuations are insignificant ($\kappa \sim \kappa_0$) and Eq. (2) reduces to the predictions of the wide-plate theory [14–16]:

$$\sigma_{lim,0}^{TFS} \sim l_x^{-2}, l_x \ll l_{th}. \tag{3}$$

---
[*]Author to whom correspondence should be addressed: arissgouros@gmail.com

[†]Present address: Center for Energy Resources Engineering, Department of Chemical and Biochemical Engineering, Technical University of Denmark, Building 229, Lyngby 2800, Denmark.

[‡]Present addresses: (i) Computation-Based Science and Technology Research Center, The Cyprus Institute, Nicosia 2121, Cyprus; (ii) Department of Materials Science & Technology, University of Crete, Vasilika Vouton, GR-71003 Heraklion, Crete, Greece.
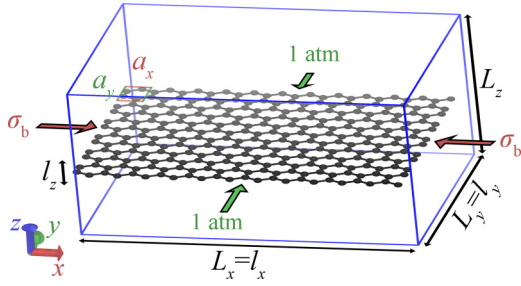
FIG. 1. Compressed graphene sheet with $(n_x, n_y) = (12, 6)$. See text for more details [49].

TABLE I. Universal coefficients of the buckling kinetics.

Quantity	Value	Unit
$\gamma_{0/L}$	2.5149	10^{-20} m^2
$U_{0\cdot L}$	900.0212	10^{-30} J m
c_{U1}	41.6257	10^{12} m^{-2} K^{-1}
c_{U2}	−0.000409	K^{-1}
$c_{\gamma 1}$	25.6131	10^{12} m^{-2} K^{-1}
$c_{\gamma 2}$	−0.000479	K^{-1}
c_{trav}	0.0093	GPa^{-1}

If, however, the sheet is large, κ increases and the resistance to buckling is enhanced:

$$\sigma_{\text{lim}}^{\text{TFS}} \sim l_x^{-2+\eta} l_{\text{th}}^{-\eta} \sim l_x^{-2+\eta} T^{\eta/2}, l_x \gg l_{\text{th}}. \qquad (4)$$

Much work has been realized in order to understand the onset of the buckling instability [19,20,37,38]; however, the kinetics of the buckling process and the effect of duration are not well understood.

We investigate the buckling kinetics of periodic graphene sheets via molecular dynamics (MD) simulations powered by a rare-event analysis framework [39]. The atomistic observables are described by the Boltzmann-Arrhenius-Zhurkov (BAZ) model, which has been extended in order to account for the scale- and temperature-dependent renormalized material parameters [40]. The simulation strategy developed herein can be used as a rigorous approach for quantifying the effect of duration and finite-size; varying these parameters can lead to very different qualitative response.

We employ an empirical force field based on first-principles calculations [41–43]. By applying the framework of linear elastic deformation [44] we retrieved analytically the 2D Lamé parameters, $\mu_0^{2D} = 130.57$ Pa m and $\lambda_0^{2D} = 71.98$ Pa m. The corresponding Young's modulus ($E_0^{2D} = 317.6$ Pa m), bulk modulus ($B_0^{2D} = 202.6$ Pa m) and Poisson ratio ($\nu = 0.216$) coincide with numerical evaluations [45] and conform with the estimations in Ref. [41]. κ_0 was determined analytically [46] as 1.86 eV. The resulting thermal wavelenth [Eq. (1)] is $l_{\text{th}} = 6.7$ nm at 300 K. Additional information regarding the force field, and the derivation of the elastic constants and bending rigidity can be found in Secs. S1–S3 of the Supplemental Material [47]).

The sheets were generated by replicating a four-atom orthogonal unit cell with dimensions $(a_x/\text{nm} \times a_y/\text{nm}) = (0.246 \times 0.426)$, n_x and n_y times along the x and y axis, respectively; e.g., see Fig. 1. The dimensions of the sheet (l) and simulation box (L) are the same along the (periodic) lateral dimensions $L_\alpha = l_\alpha = n_\alpha a_\alpha$ ($\alpha = x, y$). A vacuum gap of $L_z = 2$ nm is maintained along the (aperiodic) normal direction. The effective thickness of graphene is set to the interlayer distance in graphite; $l_z = 0.335$ nm [48].

The calculations have been realized via LAMMPS [50] with the Nosé-Hoover thermostat/barostat [51–53] and time step 1 fs. The sheets were equilibrated in the *NVT* ensemble for 0.5 ns, and then in the $NP_{xx}^{g}P_{yy}^{g}L_zT$ ensemble for 0.5 ns with $P_{xx}^{g} = P_{yy}^{g} = 1$ atm. The relation between the *system* ($P_{\alpha\beta}$) and the *local* ($P_{\alpha\beta}^{g}$) pressure tensor, $P_{\alpha\beta} = P_{\alpha\beta}^{g} l_z/L_z$, renders $P_{\alpha\beta}^{g}$

independent on the choice of L_z (vacuum gap). The simulation was continued for additional 5 ns, during which we estimated the reference dimensions ($\langle l_{x,T} \rangle, \langle l_{y,T} \rangle$).

Subsequently, the sheets experience compressive stresses (σ_b) along the loading x direction and atmospheric pressure along the y axis; i.e., $NP_{xx}^{g}P_{yy}^{g}L_zT$ ensemble where $P_{xx}^{g} = \sigma_b$ and $P_{yy}^{g} = 1$ atm (see Fig. 1). Our simulations were terminated at the time $t_{b,i}$ where the compressive strain $\varepsilon(t) = 1 - l_x(t)/\langle l_{x,T} \rangle$ reached a threshold value ε_{th}; i.e., $t_{b,i}$ is quantified as the first passage time for reaching ε_{th}. For each set of (l_x, l_y, T and σ_b) we conducted multiple simulations, each one starting with different velocity distribution and followed by a short thermalization run at atmospheric pressure for 80 ps. From the buckling times we determined the mean buckling time (t_b) and the corresponding standard error.

Setting ε_{th} to 0.03 ensures buckling in all cases examined here; it is larger than the buckling strain of the shortest sheet examined (see Sec. S4 of the Supplemental Material [47]), while it is known that buckling strain decreases with length [34,35]. t_b is insensitive to the precise value of ε_{th} because the strain increases abruptly after the emergence of the buckling (see Sec. S5 of the Supplemental Material [47]). This insensitivity becomes more apparent with increasing length. The choice of ε_{th} affects the quantification of the kinetics at extremely short time scales, commensurate with the oscillation frequency of the sheet; this regime is of minor importance since buckling is realized about instantaneously in these cases. The adoption of alternative buckling criteria based on the out-of-plane displacement of the graphene atoms yields similar results qualitatively; see Sec. S5 of the Supplemental Material [47]. Due to the lateral periodicity, the maximum wavelength of the buckling pattern equals the sheet size along the loading axis (see pre/post-buckling snapshots in Sec. S5 of the Supplemental Material [47] and the corresponding movie files). Even though the compressive experiments are stress-controlled (and not strain-rate-controlled), inertial effects are naturally incorporated in our model. One could identify an effective strain rate as $\dot{\varepsilon} \sim \varepsilon_{\text{th}}/t_b$ (e.g., compare with Eq. (4) in Ref. [39]) which is an increasing function of σ_b. The same response is observed from strain-controlled setups [54].

Figure 2 presents t_b versus σ_b at various temperatures. The black vertical line corresponds to the limiting stress at zero temperature ($\sigma_{\text{lim},0}$). A sheet will never buckle if the applied stress is lower than $\sigma_{\text{lim},0}$ (at 0 K); i.e.:

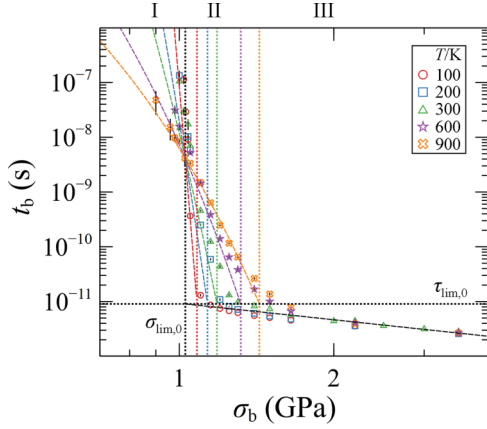$$t_b = \infty, \forall \sigma_b < \sigma_{\text{lim},0}, T = 0.$$

FIG. 2. Log-log plot of t_b versus σ_b for $l_x \sim 5.9$ nm and $l_y \sim 5.1$ nm. The black vertical (horizontal) dotted lines illustrate $\sigma_{\lim,0}$ ($\tau_{\lim,0}$) from Eqs. (9) and (14)). The colored dotted lines illustrate $\sigma_{\lim}$ from Eq. (13). The colored (black) dashed lines depict evaluations with Eqs. (12) and (15) using the parameters from Table I. The error bars depict the standard error.

According to Fig. 2, t_b decreases monotonically with σ_b and its scaling with T can be classified into three regimes: (I) $\sigma_b < \sigma_{\lim,0}$, t_b decreases with T; (II) $\sigma_{\lim,0} < \sigma_b < \sigma_{\lim}$, t_b increases with T; (III) $\sigma_{\lim} \ll \sigma_b$; t_b is T independent. $\sigma_{\lim}$ can be envisioned as a variable (renormalized) limiting stress marking the boundary between the thermally activated regime II, and the barrierless (T independent) regime III. As indicated by the vertical dotted lines, $\sigma_{\lim}$ increases with T.

According to the predictions of the continuum theory of wide plates (TWP) [14–16], $\sigma_{\lim,0}$ is insensitive to l_y and scales with the inverse square length; $\sigma_{\lim,0} \sim l_x^{-2}$. Figure 3 displays t_b against $\sigma_b l_x^2$ for graphenes with varying size. The atomistic simulations conducted here and elsewhere [20,32–36] conform to these predictions; since the limiting buckling stress (at low T) can be described accurately with the scaling law of Eq. (3).

However, with increasing T the boundary between regimes II and III ($\sigma_{\lim}$), shifts towards higher stresses, indicating that the resistance to buckling is enhanced across regime II and becomes scale-dependent. For the same T, the curves in Fig. 3 shift towards larger stresses with increasing l_x, indicating that $\sigma_{\lim} \sim l_x^{-a}$, with a being lower than 2. This response coheres with the TFS [20,26]; if the scale of the system exceeds l_{th} the buckling resistance is enhanced with increasing temperature and the scaling with length becomes weaker [(see Eq. (4)].

The long-time behavior in regime I is incompatible with the TFS since the buckled state can appear faster with increasing T. We postulate that this unexpected behavior arises because the TFS does not take into account the fluctuations about equilibrium, which become important as the sample size becomes small.

At finite temperatures, the out-of-plane fluctuations arise on either side of the sheet with the same probability. At any time, the fraction of displaced regions on either side of a sheet is the same, provided the sheet is very large. However, as the sheet size becomes smaller, it is probable that these fluctuations synchronize and occur on the same side. This kind of spontaneous bending can lead to premature buckling; i.e., given enough time the sheet can buckle even for $\sigma_b < \sigma_{\lim,0}$ (regime I; top row in Fig. 3).

With increasing width this kind of synchronization becomes rather improbable and this is reflected in the ever-increasing buckling times in Fig. 3 (from top to bottom) for
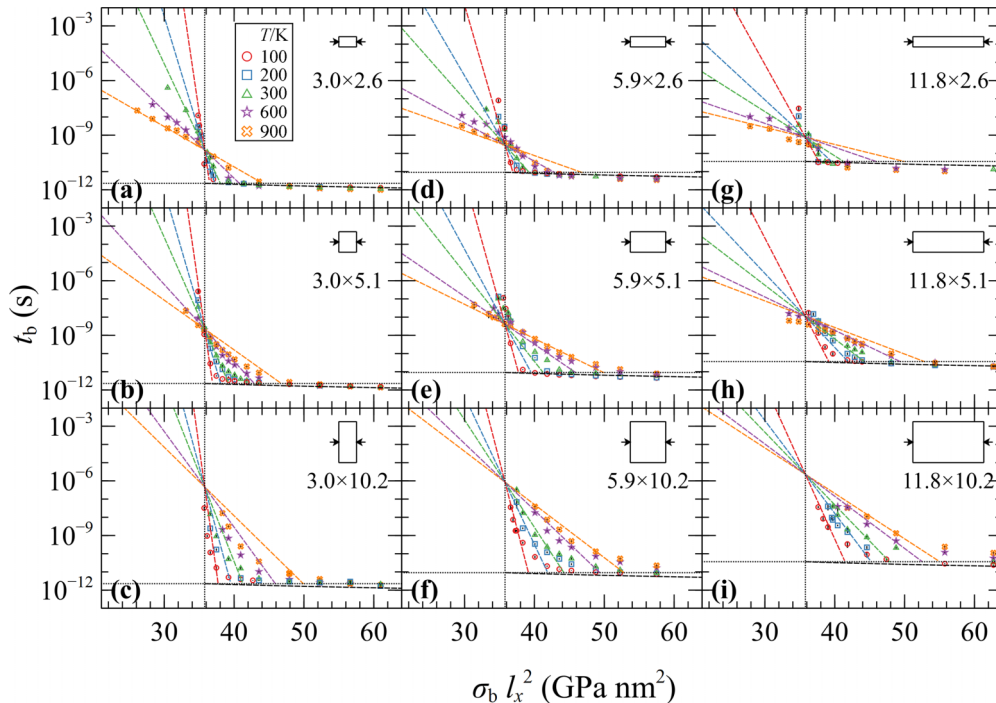

FIG. 3. Same as Fig. 2 (but with semilog axes) for the dimensions $[l_x/\text{nm} \times l_y/\text{nm}]$ illustrated in (a)–(i).

$\sigma_b < \sigma_{\text{lim},0}$. Indeed, in Figs. 3(c), 3(f), and 3(i) we notice that t_b increases precipitously with decreasing stress close to $\sigma_{\text{lim},0}$, and regime I becomes inaccessible by the simulation. In the limit $l_y \to \infty$, the aforementioned synchronization becomes impossible; thus, the resistance to buckling is enhanced with increasing temperature regardless of the duration of the experiment, in accordance with the TFS.

The premature buckling instability for low l_y is reminiscent of the predictions of the wide-column model [55] and MD simulations of loaded ribbons [33]—according to which the resistance to buckling is suppressed when the aspect ratio of the sheet is small.

We will devise a model for the buckling times, by invoking a modified version of the BAZ model [40]. According to BAZ, the mean time required to surpass an energy barrier U_0 in the presence of an external stress field σ_b is

$$t_b^{\text{BAZ}} = \tau_0 \exp\left(\frac{U_0 - \gamma_0 \sigma_b}{k_B T}\right), \tag{5}$$

where τ_0 corresponds to an oscillation period [40] or a traversal time [39]. The activation volume γ_0 corresponds to the volume of the region which is responsible for transferring the applied stress to the system. In a semilog plot, γ_0 dictates the slope of the curve, whereas the quantity $\log_{10} \tau_0 + U_0/[(\ln 10)k_B T]$ corresponds to the decimal logarithm of the buckling time for $\sigma_b = 0$. According to Eq. (5), the limiting stress for barrierless transitions is $\sigma_{\text{lim},0} = U_0/\gamma_0$. However, since $\sigma_{\text{lim},0} \sim 1/l_x^2$ [Eq. (3)], it follows that: $\gamma_0 \sim l_x^n$ and $U_0 \sim l_x^{n-2}$ with n ranging between 0 and 2. According to the fitting procedure in Sec. S6.2 of the Supplemental Material [47], the best fit is achieved for $n \sim 1$; thus, indicating that $\gamma_0 \sim l_x$ and $U_0 \sim l_x^{-1}$. We see that, in contrast to common implementations of the BAZ formula [39,40,56], γ_0 and U_0 are not material constants, but rather length-dependent quantities. By re-expressing Eq. (5) in terms of the following length-independent constants:

$$U_{0 \cdot L} = U_0 l_x = \text{const}, \tag{6}$$

$$\gamma_{0/L} = \gamma_0 l_x^{-1} = \text{const}, \tag{7}$$

we derive the modified BAZ equation shown in Eq. (8):

$$t_{b,0}^{\text{BAZ}}(T, \sigma_b, l_x) = \tau_0 \exp\left(\frac{U_{0 \cdot L} l_x^{-1} - \gamma_{0/L} l_x \sigma_b}{k_B T}\right), \sigma_b \leqslant \sigma_{\text{lim},0}. \tag{8}$$

The corresponding limiting stress shown in Eq. (9) is fully compatible with the TWP [14–16] and the TFS [20,26] (when $l_x, l_y < l_{\text{th}}$), since the $\sim l_x^{-2}$ dependence of the limiting stress arises naturally:

$$\sigma_{\text{lim},0} = \frac{U_0}{\gamma_0} = \frac{1}{l_x^2} \frac{U_{0 \cdot L}}{\gamma_{0/L}} \tag{9}$$

Equations (8) and (9) are incompatible with the TFS for l_x, $l_y > l_{\text{th}}$ and with the atomistic simulations conducted here and elsewhere [20,29,33], according to which thermal fluctuations affect the buckling stress and make it scale dependent. According to Fig. 3, the slope in regime I becomes steeper with increasing l_y (from top to bottom). The slope increases with l_x

as well, but this cannot be illustrated clearly from Fig. 3 since t_b is plotted against $\sigma_b l_x^2$. According to Eq. (9), increasing $\gamma_{0/L}$ while keeping $U_{0 \cdot L}$ constant results in a lower $\sigma_{\text{lim},0}$. The fact that the curves shift towards larger stresses with increasing area is an indication that the barrier energy increases by a larger amount than the activation volume. Therefore, according to our findings, both $\gamma_{0/L}$ and $U_{0 \cdot L}$ in Eq. (8) would have to vary with the area of the sheet in order to reproduce the buckling times in Fig. 3.

This kind of behavior can arise from a simple model for a sheet with n uncorrelated subregions, each one fluctuating towards either side of the sheet under the imposed stress. The probability that all subregions in a primary simulation box point either in the up or the down direction is $P = 2^{1-n}$. Considering that pointing in the same direction is a prerequisite for buckling to nucleate, there will be a free energy barrier of entropic origin associated with buckling commensurate to

$$U_{\text{entropic}} \sim -k_B T \ln P = n k_B T \ln 2 - k_B T \ln 2.$$

Assuming that the number of subdomains increases proportionally ($n \sim S$) with the area of the sheet ($S = l_x l_y$) we get an entropic barrier of the form:

$$U_{\text{entropic}} \sim (aS + b)T$$

with $a > 0$ and $b < 0$ being constants. The bigger the simulation box, the higher this entropic contribution to the activation energy for buckling will be. On the contrary, when the sheet is small ($n \leqslant 1$) the entropy promotes the onset of the buckling instability; the out-of-plane fluctuations (which are enhanced with increasing T) can synchronize and initiate the buckling. Discerning the effect of temperature and scale on the activation volume is not straightforward. Nonetheless, since the two are interrelated [Eq. (9)] we will assume a similar functional dependence on T and S.

By taking the two mechanisms into account we can express the renormalized, barrier energy ($U_{\cdot L}$) and activation volume ($\gamma_{/L}$) as follows:

$$\frac{U_L}{U_{0 \cdot L}} = 1 + (c_{U1}S + c_{U2})T, \tag{10}$$

$$\frac{\gamma_{/L}}{\gamma_{0/L}} = 1 + (c_{\gamma1}S + c_{\gamma2})T, \tag{11}$$

where $c_{U1}, c_{\gamma1} > 0$ (since the barrier increases with S), and $c_{U2}, c_{\gamma2} < 0$, since at low T, the energy barrier and activation volume decrease with increasing T.

We can generalize Eqs. 8 and 9 in terms of U_L and $\gamma_{/L}$ as

$$t_b^{\text{BAZ}}(T, \sigma_b, l_x, l_y) = \tau_{\text{lim},0} \exp\left(\frac{U_L l_x^{-1} - \gamma_{/L} l_x \sigma_b}{k_B T}\right), \tag{12}$$

$$\sigma_{\text{lim}} = \frac{1}{l_x^2} \frac{U_L}{\gamma_{/L}}. \tag{13}$$

Note that t_b^{BAZ} is T independent at $\sigma_{\text{lim},0}$; see proof in Sec. S7 of the Supplemental Material [47].

By following the footsteps of Ref. [39], the limiting time was set equal to the intercept of the limiting stress with the traversal time:

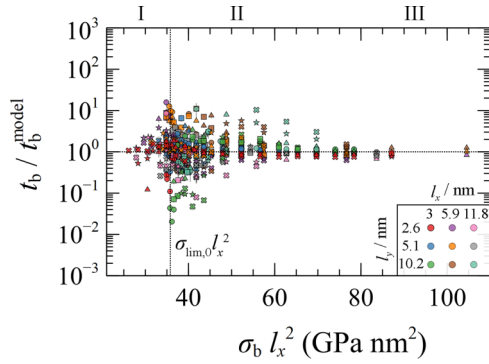$$\tau_{\text{lim},0} = \tau_b^{\text{trav}}(\sigma_{\text{lim},0}), \tag{14}$$

FIG. 4. Master plot of t_b/τ_b^{model} from Eq. (16) versus $\sigma_b l_x^2$ for $T/K = 100$ (○), 200 (□), 300 (△), 600 (☆) and 900 (×). Colors refer to sheets with different dimensions according to the table in the figure legend. The vertical (horizontal) dotted line illustrates $\sigma_{lim,0} l_x^2$ ($t_b/\tau_b^{model} = 1$).

the latter being commensurate to the time required for the graphene edges to exceed a threshold displacement $l_x \varepsilon_{th}$ in the barrierless regime. According to Fig. 2, τ_{trav} can be described very accurately by a power-law of the form:

$$\tau_b^{trav} = c_{trav}\sigma_b^{-1}. \tag{15}$$

Since the time is inversely proportional to stress (see Sec. S6.1 of the Supplemental Material [47]) and since $\sigma_{lim,0} l_x^2 = const$ (Eq. (9)), it follows that $\tau_{lim,0}/l_x^2 = const$ as well.

Accounting accurately for the intermediate regime II is not straightforward due to the gradual transition from exponential to power-law scaling behavior exhibited by the buckling time versus stress curves. Nevertheless, in order to reduce the complexity of the model, we will assume exponential scaling across regimes I and II, and a power-law dependence across regime III. In doing so, we can describe the buckling times

with the model in Eq. (16):

$$t_b^{model}(T, \sigma_b, l_x, l_y) = \begin{cases} t_b^{BAZ}, & \sigma_b \leqslant \sigma_{lim}\,(\text{regimes I and II}) \\ \tau_b^{trav}, & \sigma_b \geqslant \sigma_{lim}\quad(\text{regime III}) \end{cases}. \tag{16}$$

The model has been fitted to the buckling times from the first two rows in Fig. 3 ($l_y \leqslant 5.1$ nm) where regime I is accessible by using the Nelder-Mead method [57]; see Sec. S6.2 of the Supplemental Material [47]. The fitted coefficients reported in Table I are universal for all samples.

According to the evaluations of Eq. (12) (dashed lines in Fig. 3), the model accounts for the monotonic enhancement of the buckling stress with increasing T in regime II (conforming to the TFS). Since $c_{U1} > c_{\gamma 1}$, the barrier energy $U_{R\cdot L}$ increases at a faster pace that the activation volume $\gamma_{R/L}$; therefore, $\sigma_{lim,R} l_x^2$ in Eq. (13) is a strictly increasing function of T, cohering in this manner with the TFS. Finally, the model describes the premature buckling instability at long times (regime I). The effect becomes more apparent at low widths and this is reflected in that the factors $(c_{U1}S + c_{U2})$ and $(c_{\gamma 1}S + c_{\gamma 2})$ in Eqs. (10) and (11) become negative.

The master plot in Fig. 4 illustrates the ratio of the simulated to the fitted buckling times according to Eq. (16) for all the cases examined in Fig. 3. The model provides a fair description of the buckling kinetics across the pure exponential (I) and barrierless (III) regimes. The largest discrepancy appears in regime II, where the exponential scaling goes over to a power-law scaling and this behavior cannot be captured accurately by Eq. (12). The model can be extended in terms of introducing a more complicated expression along regime II (e.g., a stretched exponential function or various switching functions) and by allowing for sublinear scaling of the material constants with temperature [17,18,24,25], which could potentially enhance its performance when considering mesoscopic sheets where anharmonic effects become important [29].

[1] M. G. Pastore Carbone, A. C. Manikas, I. Souli, C. Pavlou, and C. Galiotis, Nat. Commun. **10**, 1572 (2019).

[2] C. Androulidakis, E. N. Koukaras, M. G. Pastore Carbone, M. Hadjinicolaou, and C. Galiotis, Nanoscale **9**, 18180 (2017).

[3] M. W. Barsoum, X. Zhao, S. Shanazarov, A. Romanchuk, S. Koumlis, S. J. Pagano, L. Lamberson, and G. J. Tucker, Phys. Rev. Mater. **3**, 013602 (2019).

[4] A. Sgouros, M. M. Sigalas, K. Papagelis, and G. Kalosakas, J. Phys. Condens. Matter **26**, 125301 (2014).

[5] S. Deng and V. Berry, Mater. Today **19**, 197 (2016).

[6] W. Zhu, T. Low, V. Perebeinos, A. A. Bol, Y. Zhu, H. Yan, J. Tersoff, and P. Avouris, Nano Lett. **12**, 3431 (2012).

[7] D. Giambastiani, C. Tommasi, F. Bianco, F. Fabbri, C. Coletti, A. Tredicucci, A. Pitanti, and S. Roddaro, Phys. Rev. Appl. **18**, 024069 (2022).

[8] P. Huang, Y. Li, G. Yang, Z.-X. Li, Y.-Q. Li, N. Hu, S.-Y. Fu, and K. S. Novoselov, Nano Mater. Sci. **3**, 1 (2021).

[9] C. Androulidakis, E. N. Koukaras, G. Paterakis, G. Trakakis, and C. Galiotis, Nat. Commun. **11**, 1595 (2020).

[10] A. P. Sgouros, C. Androulidakis, G. Tsoukleri, G. Kalosakas, N. Delikoukos, S. Signetti, N. M. Pugno, J. Parthenios, C. Galiotis, and K. Papagelis, Appl. Mater. Interfaces **13**, 4473 (2021).

[11] J. Lidmar, L. Mirny, and D. R. Nelson, Phys. Rev. E **68**, 051910 (2003).

[12] E. J. Banigan, A. D. Stephens, and J. F. Marko, Biophys. J. **113**, 1654 (2017).

[13] A. P. Sgouros, G. Kalosakas, M. M. Sigalas, and K. Papagelis, RSC Adv. **5**, 39930 (2015).

[14] S. Timoshenko and S. Woinowsky-Krieger, *Theory of Plates and Shells*, 2nd ed. (McGraw-Hill, New York, 1959).

[15] S. Timoshenko and J. M. Gere, *Theory of Elastic Stability*, 2nd ed. (Dover, Garden City, NY, 2009).

[16] D. W. A. Rees, *Mechanics of Optimal Structural Design: Minimum Weight Structures* (John Wiley & Sons, Ltd., Chichester, UK, 2009).

[17] D. R. Nelson and L. Peliti, J. Phys. Fr. **48**, 1085 (1987).

[18] P. Le Doussal and L. Radzihovsky, Phys. Rev. Lett. **69**, 1209 (1992).

[19] D. Nelson, T. Piran, and S. Weinberg, *Statistical Mechanics of Membranes and Surfaces* (World Scientific, Singapore, 2004).

[20] A. Morshedifard, M. Ruiz-García, M. J. Abdolhosseini Qomi, and A. Košmrlj, J. Mech. Phys. Solids **149**, 104296 (2021).

[21] J. H. Los and A. Fasolino, Phys. Rev. B **68**, 024107 (2003).

[22] K. V. Zakharchenko, M. I. Katsnelson, and A. Fasolino, Phys. Rev. Lett. **102**, 046808 (2009).

[23] J. H. Los, A. Fasolino, and M. I. Katsnelson, Npj 2D Mater. Appl. **1**, 9 (2017).

[24] J. A. Aronovitz and T. C. Lubensky, Phys. Rev. Lett. **60**, 2634 (1988).

[25] E. Guitter, F. David, S. Leibler, and L. Peliti, J. Phys. Fr. **50**, 1787 (1989).

[26] L. D. Landau, E. M. Lifšic, E. M. Lifshitz, A. M. Kosevich, and L. P. Pitaevskii, *Theory of Elasticity: Volume 7* (Elsevier, Amsterdam, 1986).

[27] A. K. Geim, Angew. Chem. Int. Ed. **50**, 6966 (2011).

[28] D. Akinwande, C. J. Brennan, J. S. Bunch, P. Egberts, J. R. Felts, H. Gao, R. Huang, J. S. Kim, T. Li, Y. Li, K. M. Liechti, N. Lu, H. S. Park, E. J. Reed, P. Wang, B. I. Yakobson, T. Zhang, Y. W. Zhang, Y. Zhou, and Y. Zhu, Extrem. Mech. Lett. **13**, 42 (2017).

[29] A. Fasolino, J. H. Los, and M. I. Katsnelson, Nat. Mater. **6**, 858 (2007).

[30] Z. Xu and M. J. Buehler, ACS Nano **4**, 3869 (2010).

[31] J. C. Meyer, A. K. Geim, M. I. Katsnelson, K. S. Novoselov, T. J. Booth, and S. Roth, Nature (London) **446**, 60 (2007).

[32] A. P. Sgouros, G. Kalosakas, C. Galiotis, and K. Papagelis, 2D Mater. **3**, 025033 (2016).

[33] A. P. Sgouros, G. Kalosakas, K. Papagelis, and C. Galiotis, Sci. Rep. **8**, 9593 (2018).

[34] Q. Lu and R. Huang, Int. J. Appl. Mech. **1**, 443 (2009).

[35] Y. Zhang and F. Liu, Appl. Phys. Lett. **99**, 241908 (2011).

[36] M. Neek-Amal and F. M. Peeters, Phys. Rev. B **82**, 085432 (2010).

[37] A. Košmrlj and D. R. Nelson, Phys. Rev. B **93**, 125431 (2016).

[38] A. Genoese, A. Genoese, N. L. Rizzi, and G. Salerno, Front. Mater. **6**, 26 (2019).

[39] S. V. Kallivokas, A. P. Sgouros, and D. N. Theodorou, Phys. Rev. E **102**, 030501(R) (2020).

[40] S. N. Zhurkov, Int. J. Fract. Mech. **1**, 311 (1965).

[41] G. Kalosakas, N. N. Lathiotakis, C. Galiotis, and K. Papagelis, J. Appl. Phys. **113**, 134307 (2013).

[42] G. D. Chatzidakis, G. Kalosakas, Z. G. Fthenakis, and N. N. Lathiotakis, Eur. Phys. J. B **91**, 11 (2018).

[43] Z. G. Fthenakis, G. Kalosakas, G. D. Chatzidakis, C. Galiotis, K. Papagelis, and N. N. Lathiotakis, Phys. Chem. Chem. Phys. **19**, 30925 (2017).

[44] I. E. Berinskii and A. M. Krivtsov, Mech. Solids **45**, 815 (2010).

[45] A. Thompson, https://github.com/lammps/lammps-testing/blob/master/tests/examples/elastic/in.Elastic (2023).

[46] C. Davini, A. Favata, and R. Paroni, J. Mech. Phys. Solids **104**, 96 (2017).

[47] See Supplemental Material at http://link.aps.org/supplemental/10.1103/PhysRevE.109.L023001 for parameters of the first-principles force field for graphene; Analytic determination of the elastic constants; Analytic determination of the bending rigidity; Stress-strain curve of a graphene sheet; Sensitivity to threshold strain and consideration of alternative buckling criteria; Fitting procedure; Temperature-independent buckling time at the limiting stress for barrierless transitions. The movie files 48_12_300_0.30.mp4, 24_12_300_1.06.mp4, 24_-12_300_1.10.mp4 and 24_12_300_1.20.mp4 illustrate buckling experiments of sheets with $[l_x/nm, l_y/nm, T/K, \sigma/GPa] =$ [11.8, 5.1, 300, 1.06], [5.9, 5.1, 300, 1.06], [5.9, 5.1, 300, 1.10] and [5.9, 5.1, 300, 1.20], respectively.

[48] L. A. Girifalco and R. A. Lad, J. Chem. Phys. **25**, 693 (1956).

[49] W. Humphrey, A. Dalke, and K. Schulten, J. Mol. Graph. **14**, 33 (1996).

[50] A. P. Thompson, H. M. Aktulga, R. Berger, D. S. Bolintineanu, W. M. Brown, P. S. Crozier, P. J. in 't Veld, A. Kohlmeyer, S. G. Moore, T. D. Nguyen, R. Shan, M. J. Stevens, J. Tranchida, C. Trott, and S. J. Plimpton, Comput. Phys. Commun. **271**, 108171 (2022).

[51] S. Nosé, J. Chem. Phys. **81**, 511 (1984).

[52] W. G. Hoover, Phys. Rev. A **31**, 1695 (1985).

[53] G. J. Martyna, D. J. Tobias, and M. L. Klein, J. Chem. Phys. **101**, 4177 (1994).

[54] J. W. Jiang, Sci. Rep. **5**, 7814 (2015).

[55] J. C. Houbolt and E. Z. Stowell, Critical stress of plate columns, Report/Patent No. NACA-TN-2163, 1950, https://ntrs.nasa.gov/citations/19930082777.

[56] E. Suhir and S. M. Kang, Mod. Phys. Lett. B **27**, 1330009 (2013).

[57] J. A. Nelder and R. Mead, Comput. J. **7**, 308 (1965).